J Appl Electrochem (2010) 40:1949–1956
DOI 10.1007/s10800-010-0171-1

ORIGINAL PAPER

# The influence of nanocrystalline state of iron on the corrosion inhibitor behavior in aqueous solution

**Vahid Afshari · Changiz Dehghanian**

Received: 17 December 2009 / Accepted: 4 July 2010 / Published online: 21 July 2010


**Abstract** Effect of grain size reduction on the electrochemical and corrosion behavior of iron of different grain sizes (32–320 nm) produced by direct and pulsed current electrodeposition was characterized using Tafel polarization curves and electrochemical impedance spectroscopy (EIS). The grain size of deposits was determined by X-ray diffraction (XRD) analysis and scanning electron microscopy (SEM). The most intensive first-order peak (110) of the XRD patterns was taken for detailed analysis using a Gaussian fitting curve. The electrochemical tests were carried out in electrolyte 30 mg $L^{-1}$ NaCl + 70 mg $L^{-1}$ $Na_2SO_4$ + 250 mg $L^{-1}$ $NaNO_2$ aqueous solution. It was found that the corrosion potential and corrosion current density significantly changed as the microstructure morphology was changed. Results obtained from electrochemical tests suggested that the inhibition effect and corrosion protection of sodium nitrite inhibitor in near-neutral aqueous solutions increased as the grain size decreased from submicrocrystalline to nanocrystalline. This was attributed to the excess free energy, and concomitantly the increased number of the active sites caused by higher grain boundary and triple junction content in the nanocrystalline surface, which provides sites for electrochemical activity, and effect of sodium nitrite, was more pronounced.

**Keywords** Nonocrystalline · Iron · Inhibitor · Grain size · Electrodeposition · Corrosion

V. Afshari (✉) · C. Dehghanian
School of Metallurgy & Materials Engineering,
College of Engineering, University of Tehran,
P.O. Box 11365-4563, Tehran, Iran
e-mail: Vafshari@ut.ac.ir

## 1 Introduction

The term nanomaterials includes materials with grain size between 1 and 100 nm, at least in one dimension [1–3]. Larger particles are called submicron. Nanostructure materials with significant amount of surfaces and interfaces have been attracting much interest because of their demonstrated or anticipated unique properties compared to conventional materials. The unique properties of nanocrystalline materials are derived from their large number of grain boundary regions and correspondingly large specific interphase energy compared to coarse-grained polycrystalline counterparts [4]. Magnetic and mechanical properties are examples of properties which, even for coarse-grained materials, depend on grain boundaries and other lattice defects, in spite of their tiny volume fraction [5–7]. Nanocrystallization of a coarse-grained polycrystalline material provides a new approach to improve the properties without changing chemical composition. The small grain size and the high volume fraction of grain boundaries may result in corrosion behavior different from polycrystalline materials. According to Wang and Li [8, 9] and Inturi and Szklarska-Smialowski [10] the corrosion resistance of nanocrystalline SS 304 in NaCl solution was enhanced in comparison with coarse-grained SS 304. Similarly, improved corrosion resistance of nanocrystalline N06022 in hot acid chloride solution was also reported [11]. Youssef and coworkers reported that nanocrystalline Zn coatings exhibited improved corrosion resistance in comparison to electrogalvanized steel in NaOH solution [12]. Studies have also demonstrated that nanocrystalline Ni made by electrodeposition offers superior resistance to localized corrosion [13]. The effectiveness of corrosion inhibitors is related to the extent to which they adsorb and cover the metal surface. Adsorption depends on the structure of the

inhibitor, on the surface charge of the metal, and on the type of electrolyte [14]. The objective of this study is to evaluate the beneficial effect of grain size reduction on the corrosion protection of sodium nitrite on Fe coatings in near-neutral aqueous solutions using potentiodynamic polarization and impedance measurement techniques. Possible mechanisms responsible for improved inhibition will also be discussed.

## 2 Experimental

The Fe coatings used in this study were produced via direct and pulsed current electrodeposition techniques. The volume of plating solutions used was 0.5 L. The plating baths were prepared from commercial super-grade reagents chemicals and distilled water. In the case of direct current electrodeposition, electrolyte composition was 250 g $L^{-1}$ $FeSO_4{\cdot}7H_2O$, 120 g $L^{-1}$ $(NH_4)_2SO_4$, and 30 g $L^{-1}$ $H_3BO_3$. Before electrodeposition, a small amount of $H_2SO_4$ was added to the solution to reduce the pH value to 2.2. In addition a small amount of pieces of pure iron were dipped into the solution for the reduction of $Fe^{3+}$ ions to $Fe^{2+}$ ions. The plating was performed at current densities of 600, 800, and 1000 A $m^{-2}$. The bath temperature was maintained at 60 ± 1 °C. Mechanical agitation of the electrolytes was performed with a magnetic stirrer at a rate of 600 rpm. These parameters were optimized at after initial studies in which the effect of temperature and current density on the adherence, uniformity, grain size, and current efficiency was studied. The bath composition of pulsed current electrodeposition was: 100 g $L^{-1}$ $(NH_4)_2Fe$ $(SO_4)$, 120 g $L^{-1}$ citric acid salt, 20 g $L^{-1}$ citric acid, and 30 g $L^{-1}$ boric acid. The plating parameters were: $t_{on} = 12$ ms, $t_{off} = 120$ ms, and a pulsed current density of 2000 A $m^{-2}$. Pure iron (99.99%) was used as an anode, and the substrate material was commercial low carbon steel as a cathode. Prior to depositing, the low carbon steel substrates were ground sequentially with silicon carbide papers of 400, 600, 800, 1200, 1500,2000, and 2500 grits then rinsed with distilled water. Optical microscopy was used to examine the surface of samples for scratches or pits. After an ultrasonic cleaning step in ethanol, the preparation is completed by rinsing the specimens with distilled water and drying them in warm airflow. The pretreated sample surfaces have a mirror-like finish. Just before the electrodeposition the specimens are activated in 10% $H_2SO_4$ solution at room temperature for 5 s and rinsed. The coatings thickness was fixed to about 8 μm by controlling the plating time. All the deposition experiments were duplicated, and good reproducibility was obtained. The grain size of the specimens was analyzed by X-ray diffractometry (XRD) and scanning electron microscopy (SEM), and their composition was analyzed using an X-ray energy dispersive spectrometer (EDS) attached to the SEM. X-ray diffraction studies were carried out using a Philips X'Pert-Pro instrument operated at 40 kV and 30 mA with $CoK_\alpha$ radiation ($\lambda = 0.1789$ nm) at a scan rate of 0.05° $s^{-1}$ in the range 20–130° and 0.02° step size. The full width at half maximum (FWHM) of the peak is broadened due to grain size reduction. The most intensive first-order peak (110) of the XRD patterns was taken for detailed analysis using a Gaussian fitting curve. The average grain size D was estimated according to the Scherrer equation [15]

$$D = \frac{0.9\lambda}{\beta \operatorname{Cos} \theta} \tag{1}$$

where D is the average grain size, $\lambda$ is the wavelength of the X-ray, $\theta$ is the Bragg angle for the peak, and $\beta$ is the intrinsic (true) profile full width at half maximum intensity. The $\beta$ parameter was calculated using the Gaussian–Gaussian (GG) relationship [16, 17]

$$\beta_{exp}^2 = \beta^2 + \beta_{ins}^2 \quad \text{(GG)} \tag{2}$$

where $\beta_{exp}$ and $\beta_{ins}$ are the full width of the diffraction line measured at half maximum intensity of experimental and instrumental profiles, respectively. The annealed pure iron (99.99%) with average grain size of 300 μm was used as reference sample to determine instrumental broadening corrections. The surface microstructure and grain size of the annealed sample were examined by the optical microscopy using polarizing microscope model Eclipse 50i POL. For electrochemical experiments, non-deaerated solution of 30 mg $L^{-1}$ sodium chloride + 70 mg $L^{-1}$ sodium sulfate was prepared using analytical grade reagents and distilled water in the presence of sodium nitrite at 250 ppm concentration. The volume of cell used in electrochemical experiments was 200 cc. All the chemical solutions were freshly prepared, and the temperature of the solutions during tests was kept at 25 °C. Duplicate electrochemical measurements were made with a conventional three-electrode cell. A saturated calomel electrode (SCE) was used as a reference electrode. The auxiliary electrode was a platinum foil with total surface of 2 $cm^2$. The iron coating specimens were used as working electrode in the form of coupons with exposed area of 2.25 $cm^2$. EIS measurements were conducted at the open circuit potential after immersion of a sample into the solution for 30 min. The applied potential amplitude was 5 mV, and the frequency ranged from 100 KHZ to 0.01 HZ using a 1260 Solarton frequency response analyzer (FRA). The collected data were analyzed with an equivalent circuit using "ZView2" software. Potentiodynamic polarization curves were acquired, and the corrosion potential ($E_{corr}$) and corrosion current density ($i_{corr.}$) were determined using the Tafel extrapolation method. The

polarization scanning was started at 0.25 $V_{SCE}$ below corrosion potential and scanned upward to an anodic potential of 0.8 $V_{SCE}$ above the corrosion potential, and measurements were made at a linear sweep scan rate of 2 mV $s^{-1}$ using potentiostat MODEL 273(EG&G) with "Softcorr 352" software. Prior to the measurements, the working electrode was allowed to stabilize in the electrolyte for 1 h. Potential versus current density characteristics of the specimens were monitored. All polarization tests were performed after each corresponding EIS test.

## 3 Results and discussion

Figure 1 shows the XRD patterns of the iron coatings at different grain sizes produced by the direct and pulse electrodeposition. For comparison, the XRD pattern of a reference sample (annealed iron) is also shown. It can be observed that the crystal structure of the coatings is pure bcc iron, and no characteristic peaks of other phases were recorded. The grain sizes of the iron coatings varied between 320 and 32 nm. The grain sizes for the electrodeposited iron films and current condition are listed in Table 1. For the nano-grained specimen, the width of the peaks was significantly broadened due to the ultrafine grain size (32 nm). The crystallographic texture changes from a strong (110) fiber texture to a (110) (211) double fiber texture for pulse plated iron nanocrystals. In Fig. 1, the peak broadening of the samples is not entirely clear, because the FWHM is small. In order to have a better distinction between the samples, the intensity of (200) reflection for iron coatings with various grain sizes is presented in Fig. 2. It can be seen that the peak width increases by decreasing the grain size. Figure 3 shows the SEM micrographs of the electrodeposited iron films. By picking out over 50 particles in each sample, histograms of the grain sizes were obtained. Typical histograms are shown in Fig. 4. The SEM image of the nanocrystalline iron sample also provides evidence that the grain size is of the nanoscale, but with a bigger size value. The grain size from XRD presents an average value for the surface layer, while the SEM images in Fig. 3 only show the grains at a particular location. The uniform ultrafine grains were mostly equiaxed crystallites interconnected by incoherent interfaces. The optical microscopy image of the annealed iron sample is shown in Fig. 5. The chemical compositions of the electrodeposited iron films were determined using EDS. The iron content in the electrodeposited coating samples was ~100 atomic weight percent (at.%) measured by EDS (Fig. 6). Potentiodynamic polarization curves for the different specimens in the electrolyte 30 mg $L^{-1}$ NaCl + 70 mg $L^{-1}$ $Na_2SO_4$ + 250 mg $L^{-1}$ $NaNO_2$ aqueous solution are shown in Fig. 7. The corrosion parameters were extracted from the polarization curves using a commercial software (EG and G Model 273, Softcorr 352) and summarized in Table 2. It was established that the corrosion potential and corrosion current density were changed significantly as the microstructure was changed. These results show that the polarization curves exhibit more noble corrosion potentials and lower corrosion rates with a decrease in grain size. This behavior was probably due to the more inhibitor adsorption and formation of a passive film on the metal surface. The passive film caused a barrier

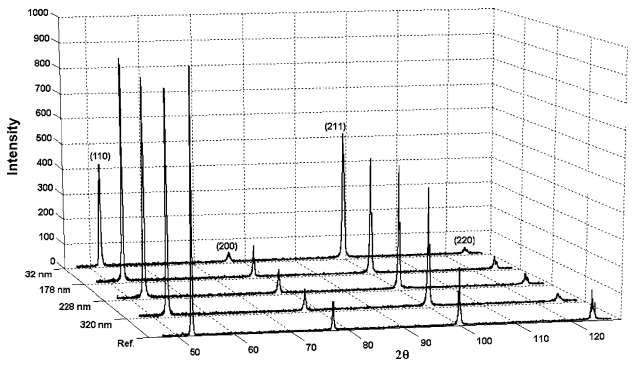


**Fig. 1** XRD Patterns of annealed and Fe coatings at different grain size

**Table 1** Treatment conditions and average grain size of various specimens

| Sample | Current density (A $m^{-2}$) | Current | Grain size (nm) |
|---|---|---|---|
| 1 | 2000 | Pulsed | 32 |
| 2 | 1000 | Direct | 178 |
| 3 | 800 | Direct | 228 |
| 4 | 600 | Direct | 320 |

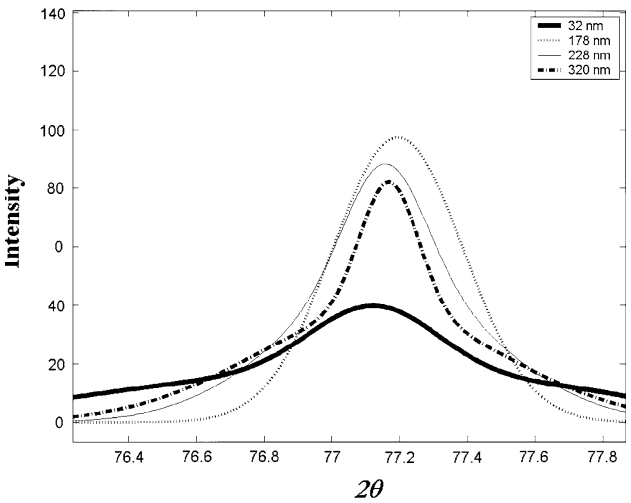


**Fig. 2** The Gaussian peak shape function of the (200) reflection peaks of Fe coatings at different grain size

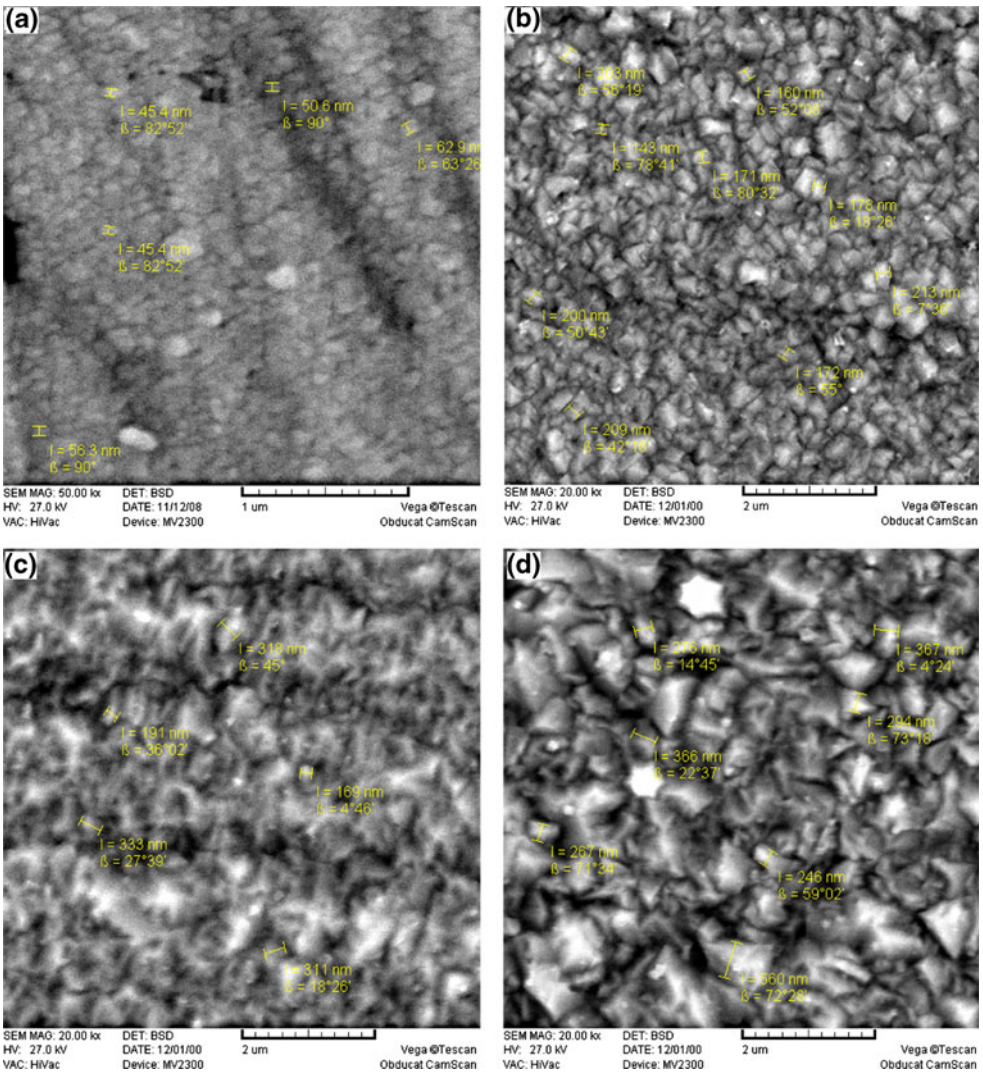


**Fig. 3** SEM images of Fe-electrodeposited specimens. Condition of deposition mentioned in Table 1; **a** sample 1, **b** sample 2, **c** sample 3, **d** sample 4

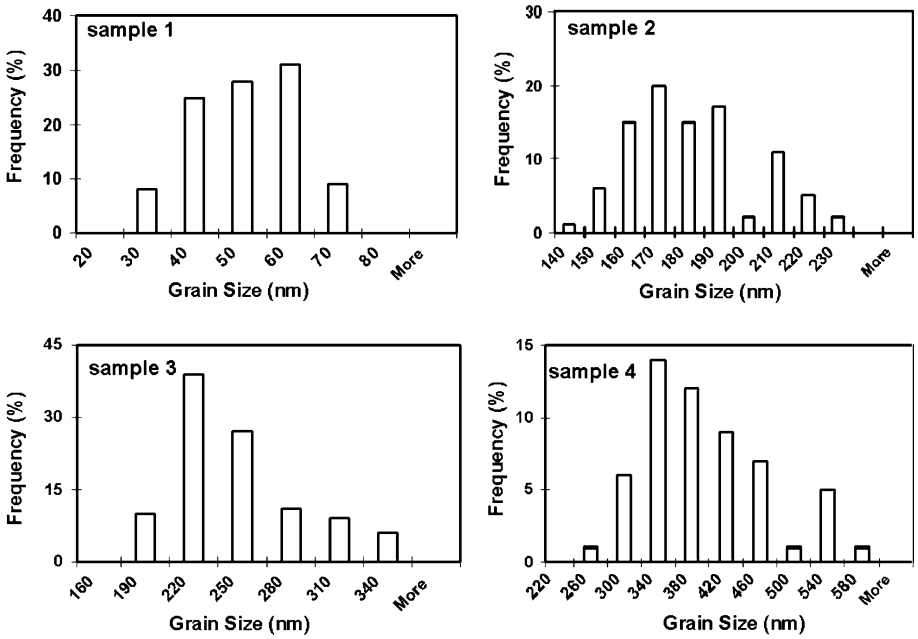


**Fig. 4** Histogram of grain size of sample 1, 2, 3, 4

effect for charge transfer of anodic reactions and markedly decreased the corrosion rate. The polarization curve of the nanocrystalline iron sample showed a passivity behavior. The scan performed on nanocrystalline iron sample exhibits several distinct characteristics: (i) A fluctuation region between −0.22 to −0.14 $V_{SCE}$, (ii) a slow dissolution regime or anodic current varies slightly in the potential range of −0.15 to 0.16 $V_{SCE}$ with a maximum current density of $3.16 \times 10^{-6}$ A $cm^{-2}$, and (iii) a transpassive regime starting at the potential of approximately 0.17 $V_{SCE}$. The polarization curves distinctively changed with increasing the grain size of the specimens. The $E_{corr}$ shifted slightly to a more negative potential, and the transition peaks underwent various changes. The corrosion current density of nanocrystalline iron coating (with average grain size of 32 nm) was lower in comparison of submicrocrystalline specimens. This lower current density was attributed to the higher grain boundary density, and triple junction content in the nanocrystalline specimen, which provides sites for electrochemical activity, and effect of sodium nitrite, was more pronounced. Also, the texture changes from (110) to (211) could lead to growth of free energy and number of active sites on the surface of nanocrystalline iron and enhance chemical interaction between iron surface and sodium nitrite. However, this difference in current density diminishes at higher potentials (0.5 $V_{SCE}$) at which the overall dissolution rate overwhelms the structure-controlled dissolution rate observed at lower potentials. The fluctuation in the anodic polarization curves before reaching a certain potential in nanocrystalline iron curve may be due to variation in the concentration of the products of the anodic reaction in the solution which will cause screening a considerable portion of electrode surface and sharply increasing the current on the free part of the surface. In the presence of sodium nitrite, the metal surface develops a diffusion barrier layer of reaction products on the surface, which is referred to as a passive film. The effect of nitrite ions on passivation can be

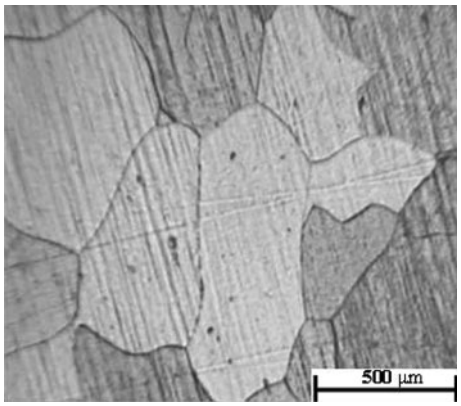


**Fig. 5** Optical image of the coarse-grained Fe specimen (annealed state)

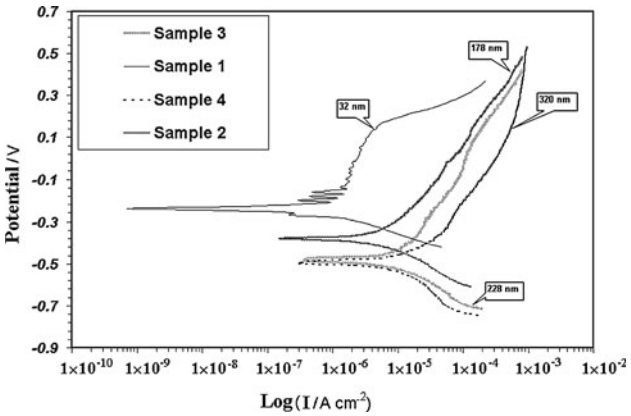


**Fig. 7** Potentiodynamic polarization curves in 30 mg $L^{-1}$ NaCl + 70 mg $L^{-1}$ $Na_2SO_4$ + 250 mg $L^{-1}$ $NaNO_2$ aqueous solutions

**Fig. 6** EDS result of nanocrystalline Fe deposit (sample 1)

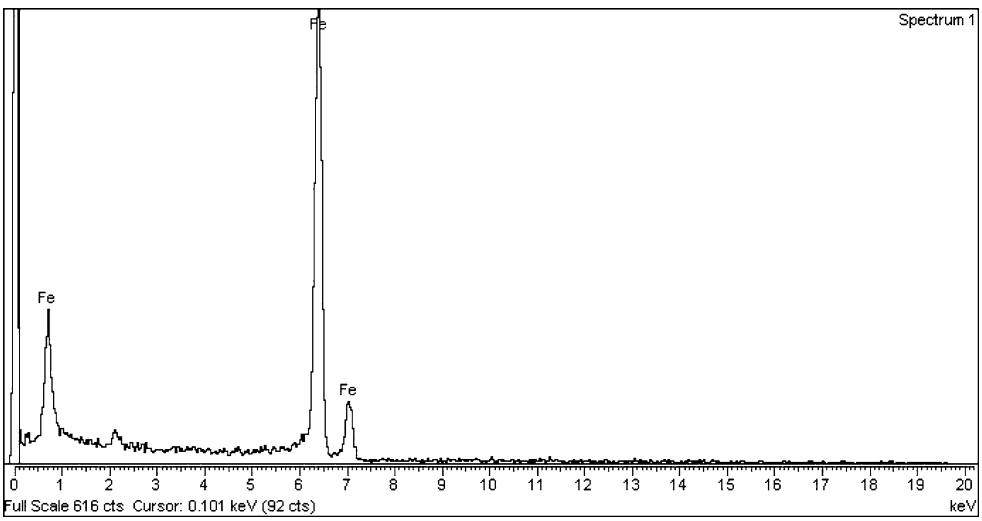

**Table 2** Tafel polarization parameter values in 30 mg $L^{-1}$ NaCl + 70 mg $L^{-1}$ $Na_2SO_4$ + 250 mg $L^{-1}$ $NaNO_2$ aqueous solution

| Sample | $\beta_a$ (mv decade$^{-1}$) | $\beta_c$ (mv decade$^{-1}$) | $E_{corr}$ (V vs. SCE) | $i_{corr}$ (A cm$^{-2}$) |
|---|---|---|---|---|
| 1 | 520 | 110 | −0.243 | $6.02 \times 10^{-7}$ |
| 2 | 312 | 152 | −0.393 | $2.88 \times 10^{-6}$ |
| 3 | 260 | 140 | −0.482 | $1.09 \times 10^{-5}$ |
| 4 | 180 | 168 | −0.496 | $1.17 \times 10^{-5}$ |

explained by adsorption of these ions, which reduces the free energy of the system and impedes the passage of ion-atom of iron from the lattice into the solution. The resistance of this film to dissolution is related to their physical and chemical nature, which determines the corrosion resistance of the metal. The inhibition effect of nitrite ions may be related to the fact that a $Fe_2O_3$ oxide film forms on the iron surface, thereby impeding the process of anodic dissolution; the formation of ferric oxides with the participation of nitrite ions takes place according to the following reactions [18]:

$$NaNO_2 \rightarrow Na^+ + NO_2^- \tag{3}$$

$$6Fe(OH)_2 + NO_2^- \rightarrow 3(\gamma - Fe_2O_3) + NH_4^+ + 3H_2O + 2OH^- \tag{4}$$

The positive shift of the open circuit potential by decreasing the grain size of the specimens is thought to be the result of the presence of more active atoms on the surface which will take part in reaction and produces a better protective passive film on the surface. The adsorption behavior of a corrosion inhibitor is a major factor for its protective properties. Adsorption is a surface phenomenon exhibited by solids which consists of the adhesion in an extremely thin layer of the molecules of gases, liquids, or of dissolved substances with which they are in contact. The adsorption of an inhibitor, I, on an electrode surface in aqueous solutions should be considered as a place for exchange reaction.

$$I_{sol} + n(H_2O)_{ads} = I_{ads} + n(H_2O)_{sol} \tag{5}$$

where $n$ is the number of water molecules displaced by one inhibitor molecule. The displacement of pre-adsorbed water molecules by adsorbing inhibitor molecules is generally considered the fundamental step of inhibition. The ability of the inhibitor to replace water molecules depends on the electrostatic interaction between the metal and the inhibitor. The interaction first started on surface crystalline lattice defects, and nanocrystal materials have a high density of grain boundaries and dislocations inside grains [19]. Hence, it is believed that the nanocrystal electrodeposited iron coating has a high density of active sites for inhibitor adsorption, which leads to a high fraction of passive layers and low corrosion rates. The nanostructure coating contains an appreciable volume fraction of interphase or grain boundary regions (analogously to the surface region of nanoparticles) and correspondingly large specific interphase energy. The excess free energy ($G_{excess}$) per unit volume of a nanocrystalline solid has the form

$$G_{excess} = \alpha d^{-1} + \beta d^{-2} + \gamma d^{-3} \tag{6}$$

where $d$ is the grain diameter, $\alpha$, $\beta$, and $\gamma$ are constant incorporating geometrical factors, $\alpha$ being proportional to the grain boundary excess free energy per unit area, $\beta$ to the junction energy per unit length, and $\gamma$ to the vertex energy [20]. A decrease in the corrosion current density could be largely attributed to the formation of a higher integrity passive film on the nanocrystalline surface. The large specific surface area of nanocrystalline and concomitantly large specific surface energy; hence surface sensitive properties (like catalytic activity) are enhanced [21–24] and process where the surface energy is the driving force are facilitated [25–27]. The impedance spectrum diagrams obtained for the frequency range from 100 kHZ to 10 mHZ at the open circuit potential are also shown in Fig. 8. All EIS diagrams show only one capacitive loop, which indicates that charge transfer, is the major controlling factor. However, they are not perfect semicircles; this has been attributed to microscopic fluctuations of the surface [28]. From the complex plane plots, the charge-transfer resistance ($R_{ct}$) was calculated from the intercept of the semicircle on the real axis in low frequency limits of the measured impedance spectra, and the double-layer

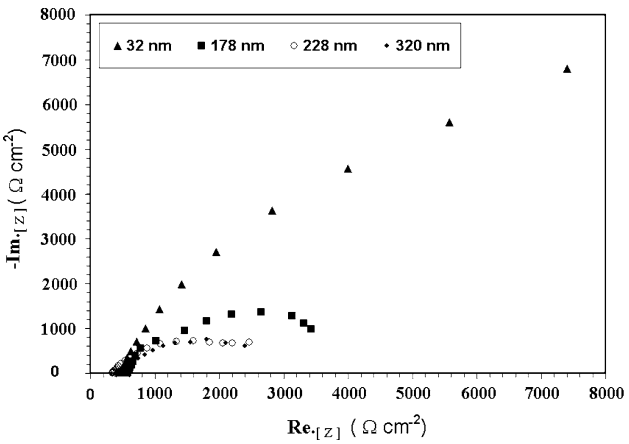


**Fig. 8** Complex plane plots of iron of different grain sizes in 30 mg $L^{-1}$ NaCl + 70 mg $L^{-1}$ $Na_2SO_4$ + 250 mg $L^{-1}$ $NaNO_2$ aqueous solution

capacitance was then calculated using the following equation:

$$C_{dl} = \frac{1}{2\pi f_{max} R_{ct}} \quad (7)$$

It is obvious that the interception of the semicircle with the abscissa at the low frequency end shifted toward the left side which may be due to an increase of the grain size, inferring that charge-transfer resistance is decreased by increasing the grain size. The atoms at grain boundary have high energies; they may take part in the reaction first. The larger the volume fraction of grain boundary, the more the active atoms on the iron surface, which results in increasing the inhibitor adsorption. Each spectrum was analyzed using a best fit to the equivalent circuit shown in the Fig. 9. The circuit includes the solution resistance, Rs, in series with one RC time constant $\tau = R_{ct}$CPE, representing the resistance and constant phase element (CPE) of the passive film. In the mathematical analysis of impedance diagrams, a CPE was substituted for modeling the capacitive behavior of the spectra in order to fit better the depressed semicircles, due to microscopic fluctuations of the surface [28].

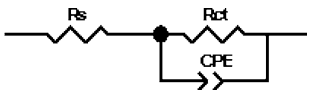


**Fig. 9** The equivalent electrical circuit modeling of impedance spectrums

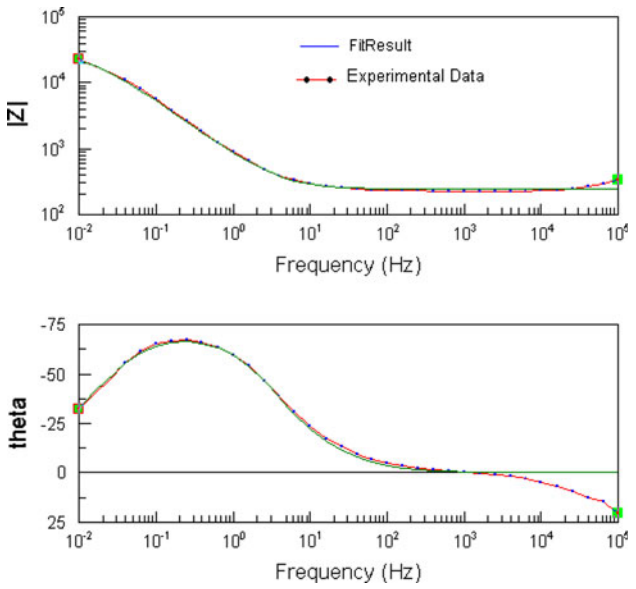


**Fig. 10** A comparison between experimental impedance data for nanocrystalline Fe deposit (sample 1) exposed to 30 mg $L^{-1}$ NaCl + 70 mg $L^{-1}$ $Na_2SO_4$ + 250 mg $L^{-1}$ $NaNO_2$ aqueous solution and the results of analysis with ZView2 (Bode graphs, magnitude and phase angle vs. frequency)

**Table 3** Impedance parameter values in 30 mg $L^{-1}$ NaCl + 70 mg $L^{-1}$ $Na_2SO_4$ + 250 mg $L^{-1}$ $NaNO_2$ aqueous solution

| Sample | $R_s$ (Ω) | $R_{ct}$ (Ω $cm^2$) | $C_{dl}$ (μF) |
|---|---|---|---|
| 1 | 241 | 31525 | 263 |
| 2 | 569 | 4512 | 366 |
| 3 | 324 | 2821 | 606 |
| 4 | 415 | 2726 | 1815 |

The impedance of a constant phase element is given as follows

$$Z_{CPE} = \frac{1}{Qs^{\alpha f}} \quad (8)$$

where $Q$ is the CPE parameter, αf is the CPE exponent (phase shift), $s = i\omega$ and $\omega$ is the angular frequency ($\omega = 2\pi f$, where f is the AC frequency), and i here is the imaginary unit. When the value of αf is 1, the CPE behaves like an ideal double-layer capacitance ($C_{dl}$) [29–32]. The correction of capacity to its real values is calculated from

$$C_{dl} = Q(\omega_{max})^{\alpha f - 1} \quad (9)$$

where $\omega_{max}$ is the frequency at which the imaginary part of impedance ($-Z_i$) has a maximum value [33]. A typical comparison of the experimental and the fitted data in Bode plot was displayed in Fig. 10. It can be seen that the simulated curve basically follows the experimental data at the most of measurement frequencies. Therefore, the experimental data are suitably fitted with the equivalent circuit shown in Fig. 9. The corrosion kinetics parameters such as $R_{ct}$ and $C_{dl}$ were obtained from the ac-impedance data using an appropriate model (ZView2 software). The results are presented in Table 3. It was found that the charge-transfer impedance was increased as the double-layer capacitance was decreased with the gradual reduction of iron grain size. This may be due to a decrease in local dielectric constant and/or an increase in the thickness of the electrical double layer. It is suggested that active sites of nanostructure surfaces promote the adsorption of nitrite ions and hence increasing the degree of coverage on the iron surface. These results are in good agreement with the results obtained from polarization measurements shown in Table 2.

## 4 Conclusions

Based on the results obtained from this research work, the following conclusions can be drawn:

(1) The crystal grain size plays an important role in the inhibition effect. The corrosion resistance of iron in electrolyte 30 mg $L^{-1}$ NaCl + 70 mg $L^{-1}$

$Na_2SO_4 + 250$ mg $L^{-1}$ $NaNO_2$ aqueous solution considerably increased as the grain size decreased from submicrocrystalline to nanocrystalline.

(2) The nanocrystal electrodeposited iron coating has a high density of nucleation sites to encourage the adsorption of nitrite ions, which leads to a high fraction of passive layers and low corrosion rates.

(3) Electrochemical impedance spectroscopy results indicated that for the nanocrystalline structures, the charge-transfer resistances in the presence of inhibitor are reasonably increased and its capacitances were decreased when compared to the coarse morphology results. This can be attributed to a decrease in local dielectric constant or an increase in the thickness of the electrical double layer.

## References


1. Gleiter H (1982) Mater Sci Eng 52:91–131
2. Gleiter H (1995) Nanostruct Mater 6(1–4):3–14
3. Gleiter H (2000) Acta Mater 48:1–29
4. Tjong SC, Chen H (2004) J Mater Sci Eng 45(1–2):1–88
5. Szpunar B, Aus M, Cheung C, Erb U, Palumbo G, Szpunar JA (1998) J Magn Magn Mater 187(3):325–336
6. Wolf H, Guan Z, Lauer S, Natter H, Schmelzer M, Hempelmann R, Wichert T (2000) Mech Alloy Nanocryst Mater 343(3): 847–852
7. Zahi S, Hashim M, Daud AR (2004) J Magn Magn Mater 308(2):177–182
8. Wang XY, Li DY (2003) Wear 255(7–12):836–845
9. Wang XY, Li DY (2002) Electrochim Acta 47(24):3939–3947
10. Inturi RB, Szklarska-Smialowski Z (1992) Corrosion 48(5): 398–403
11. Raja KS, Namjoshi SA, Misra M (2005) Mater Lett 59:570–574
12. Kh MS, Youssef CC, Koch PS, Fedkiw (2004) Corros Sci 46(1):51–64
13. Shriram S, Mohan S, Renganathan NG, Venkatachalam R (2000) Trans Inst Met Finish 78(5):194–197
14. Rozenfeld IL (1981) Corrosion inhibitor. McGraw-Hill, New York
15. Cullity BD (1978) Elements of X-ray diffraction, 2nd edn. Addison-Wesley, Reading, pp 281–285
16. Klug HP, Alexander LE (1974) X-ray diffraction procedures for polycrystalline and amorphous materials, 2nd edn. Wiley, New York, pp 618–687
17. Jiang HG, Ruhle M, Lavernia EJ (1999) J Mater Res 14:549–559
18. Joseph C, Becker E, Nason A (1970) Proc Third Eur Symp Corr Ihib. Univ Ferrara, 791
19. Balyanov A, Kutnyakova J, Amirkhanova NA (2004) Scripta Mater 51:225
20. Greer AL (1993) Mechanical properties and deformation behavior of materials having ultra-fine microstructures. Springer, New York, pp 53–77
21. Daniel MC, Astruc D (2004) Chem Rev 104:293–346
22. Lopez N, Norskov JK (2003) Abs Paper Am Chem Soc 225:U688–U688
23. Sommer WJ, Crne M, Weck M (2007) ACS J Surf colloids 23(24):11991–11995
24. Zhai S, Zhang Y, Shi X, Wu D, Sun YH, Shan Y, He MY (2004) Catal Lett 93:225–229
25. Bowen P, Carry C (2002) Powder Technol 128:248–255
26. Goujon C, Goeuriot P (2001) Mater Sci Eng A 315:180–188
27. Nihara K (1991) Nippon Seramikkusu Kyokai Gakujutsu Ronbunshi. J Ceram Soc Jpn 99:974–982
28. Moretti G, Guidi F, Grion (2003) Corros Sci 46:387
29. Popova A, Sokolova E, Raicheva S, Christov M (2003) Corros Sci 45:33
30. Gohr H, Schaller J, Schiller CA (1993) Electrochim Acta 38:1961
31. Kliskic M, Radosevic J, Gudic S, Katalinic V (2000) J Appl Electrochem 30:823
32. Babic-Samardzija K, Hackerman N (2006) Anti-Corros Method Mater 53(19)
33. Mohana KN, Badiea AM (2008) Corros Sci 50:2939–2947